Achieving equal fatigue strength to base material in a friction stir welded 5083-H19 aluminium alloy joint

B. B. Wang, P. Xue, B. L. Xiao, W. G. Wang, Y. D. Liu & Z. Y. Ma

Published online: 18 Jun 2019.

Submit your article to this journal 🖉

Article views: 94

View related articles 🔾

View Crossmark data 🗷

Check for updates

Achieving equal fatigue strength to base material in a friction stir welded 5083-H19 aluminium alloy joint

B. B. Wang[a,b], P. Xue[b], B. L. Xiao[b], W. G. Wang[b], Y. D. Liu[a] and Z. Y. Ma[b]

[a] School of Materials Science and Engineering, Northeastern University, Shenyang, People's Republic of China; [b] Shenyang National Laboratory for Materials Science, Institute of Metal Research, Chinese Academy of Sciences, Shenyang, People's Republic of China

ABSTRACT

By using a low rotation rate of 200 rpm with additional water cooling, a friction stir welded (FSW) joint with equal fatigue strength to the base material (BM) was obtained in 5083Al-H19 rolled plates due to the significantly decreased softening and the residual stress effect. Though the hardness value in the heat affected zone (HAZ) was a little lower than that of the BM, the decreased tensile effect of the residual stress in the HAZ greatly improved the fatigue performance, which was even higher than that of the BM, so the final fracture occurred at the BM. This study provides an effective strategy to enhance the fatigue performance of the FSW joints.

Introduction

5xxx series Al alloys are widely used for structural components in the aerospace and automotive areas, due to their excellent properties, such as good corrosion resistance, good weldability and high specific strength. Welding is an indispensable and important process for structure manufacturing. Friction stir welding (FSW), as a solid-state joining process, exhibits various advantages compared to the conventional fusion welding techniques [1]. However, FSW still creates an obviously softened zone in the joints of work-hardened and precipitation-hardened Al alloys at high heat input condition. In order to decrease the heat input during FSW, reducing the rotation rate and/or increasing the welding speed were usually used, but the effects were not so satisfactory [2].

In addition to changing the rotation rate and welding speed, additional cooling is an effective method of reducing the heat input and improving the strength of the FSW joints [3–6]. Sharma et al. [4] studied the effect of additional cooling on the microstructure and mechanical properties of FSW 7039 Al alloy joints with different cooling mediums including compressed air, liquid nitrogen and water. They reported that water exhibited the best cooling effect in the above cooling mediums, leading to obviously enhanced mechanical properties of the FSW joints. Meanwhile, Xue et al. [3] and Zeng et al. [5] obtained the FSW joints with near-equal strength to the base metal (BM) in cold-rolled pure copper and 6061-T6 Al alloy, respectively, by using the additional water cooling. Therefore, FSW

with additional water cooling is a highly efficient and low-cost welding method of achieving high-property FSW joints.

In these previous studies, the static tensile behaviours were mainly investigated. Actually, fatigue property is more important in industrial applications, which is always treated as the final criterion for the application of one new material or structure. Usually, high-cycle fatigue strength is the first concern in the practical application. Due to the complex microstructures of the FSW joints, there are many factors affecting the fatigue behaviour of the joint, such as welding defects, inhomogeneous microstructure and residual stress. When welding with an improper FSW parameter, the appearance of the welding defects would result in a reduction in crack initiation life under fatigue loading, and the fatigue strength was significantly decreased [7,8].

For defect-free FSW joints, the fatigue crack initiation is known to be associated with the residual stress and microstructure evolution around the welded zone [9]. Generally, the compressive residual stress induces low fatigue crack growth rates and the tensile residual stress accelerates the crack growth rates, resulting in a reduced fatigue strength of the FSW joint [10]. Due to the inhomogeneous microstructure of the FSW joints, the fatigue deformation would vary with varied microstructures. It is generally believed that fatigue crack is likely to initiate by the local deformation in the softened area originating from the annealing effect during the FSW process [11]. Therefore, how to improve

the hardness and strength of the softened zone is the critical factor for obtaining high fatigue strength of the FSW joints.

In our previous study, the hardness and strength of the softened zone were improved by adjusting the welding parameters, and FSW joint with near equal tensile strength to the BM was successfully achieved on a work-hardened Al alloy [12]. However, it is still unclear if the fatigue strength will be improved as well. In this work, a typical work-hardened 5xxx series Al alloy – 5083 Al with H19 state was chosen as the target BM for FSW investigation with additional water cooling. The aim of this study is (a) to achieve a high fatigue strength FSW joint of 5083-H19 Al alloy and (b) to elucidate the fatigue crack initiation and fracture mechanisms during the cyclic deformation process.

Base material and methods

2.8-mm-thick 5083Al-H19 plates, which were cold rolled without annealing, were used as the BM. Plates with a length of 300 mm and a width of 70 mm were butt welded along the rolling direction using a FSW machine with a tool tilt angle of 3 deg. Normal FSW (air cooling) was conducted at a welding speed of 100 mm/min with a tool rotation rate of 200 rpm, defined as A-200. In order to reduce the heat input, FSW was performed with the same welding parameters under additional water cooling, and the FSW joints were defined as W-200. The 5083 plates were fixed in a water tank with inlet and outlet. The velocity of water was about 7 L min^{-1}, and the thickness of water layer in the tank was about 30 mm during FSW. A FSW tool with a concave shoulder 12 mm in diameter and a conical threaded pin 4 mm in diameter and 2.6 mm in length was used.

The specimens for microstructural examinations were machined perpendicular to the FSW direction. Microstructural characterisation and analysis were carried out using optical microscopy (OM), scanning electron microscopy (SEM) and transmission electron microscopy (TEM). The specimens for OM observation were ground, polished, and then etched in a solution of 2 g NaOH and 100 ml H_2O for about 2-3 min. TEM foils were prepared by double-jet electrolytic polishing using a solution of 30 ml HNO_3 and 70 ml CH_3OH at 248 K under a potential of 12 V.

Vickers microhardness measurement was conducted on the cross-section perpendicular to the welding direction under a load of 200 g with a holding time of 15 s. The microhardness profiles were obtained along the mid-thickness of the cross-section of the FSW joints at an interval of 1 mm. The tensile specimens, with a gauge length of 40 mm and a gauge width of 6 mm, were machined perpendicular to the FSW direction. Uniaxial tensile tests were carried out at room temperature at an initial strain rate of 1×10^{-3} s^{-1}.

High-cycle fatigue tests were conducted using an Instron fatigue system (Instron 8872) with the same specimen dimension and preparation method as the tensile specimen. A sinusoidal load-time function with a frequency of 30 Hz and a stress ration R = 0.1 was used. All the specimens were ground and polished before fatigue tests and the tests were under room temperature and laboratory air conditions.

Results and discussion

Microstructure and tensile properties

Figure 1 shows the cross-sectional macrostructures of the FSW 5083Al-H19 joints. No porosity and tunnel defects were detected in the joints under both FSW parameters used in this study. Through the macrostructures of the FSW joints, three distinct zones were discernible: nugget zone (NZ), thermo-mechanically affected zone (TMAZ), and heat affected zone (HAZ). A continuous 'S' shaped line can be seen in the NZ of the FSW joint, which was known as the 'S' line. Sato et al. [13] found that the 'S' line in the FSW joint of Al alloy was mainly composed of many fine oxide particles coming from the initial oxide layer on the butt surface. The 'S' line was distributed in the NZ for A-200 sample, and when applying the additional water cooling, more oxide layers were deposited on the advancing side (AS) of the NZ. Though the material flow was restricted in the NZ due to the decreased peak temperature under additional water cooling [14], no unbonded root defects were observed.

Figure 2 shows the TEM microstructures of the BM and the NZs at both FSW parameters. The BM exhibited a typical heavily cold-rolled characteristic, and the grains were elongated clearly along the rolling direction, with a width of only about 300 nm (Figure 2(a)). Meanwhile, a very high density of dislocations was observed in the severely deformed grains. For the A-200 sample, many precipitates were observed in the NZ, which were mainly distributed at grain interior or grain boundaries from the image shown in Figure 2(b). 5083 Al alloy is a solution-strengthened Al alloy with supersaturated solid solutions condition. It has been
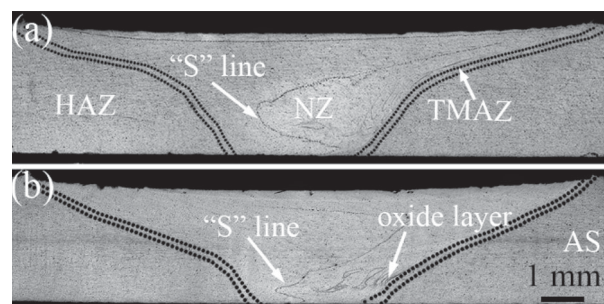

Figure 1. Cross-sectional macrostructures of FSW joints: (a) A-200 sample, (b) W-200 sample.
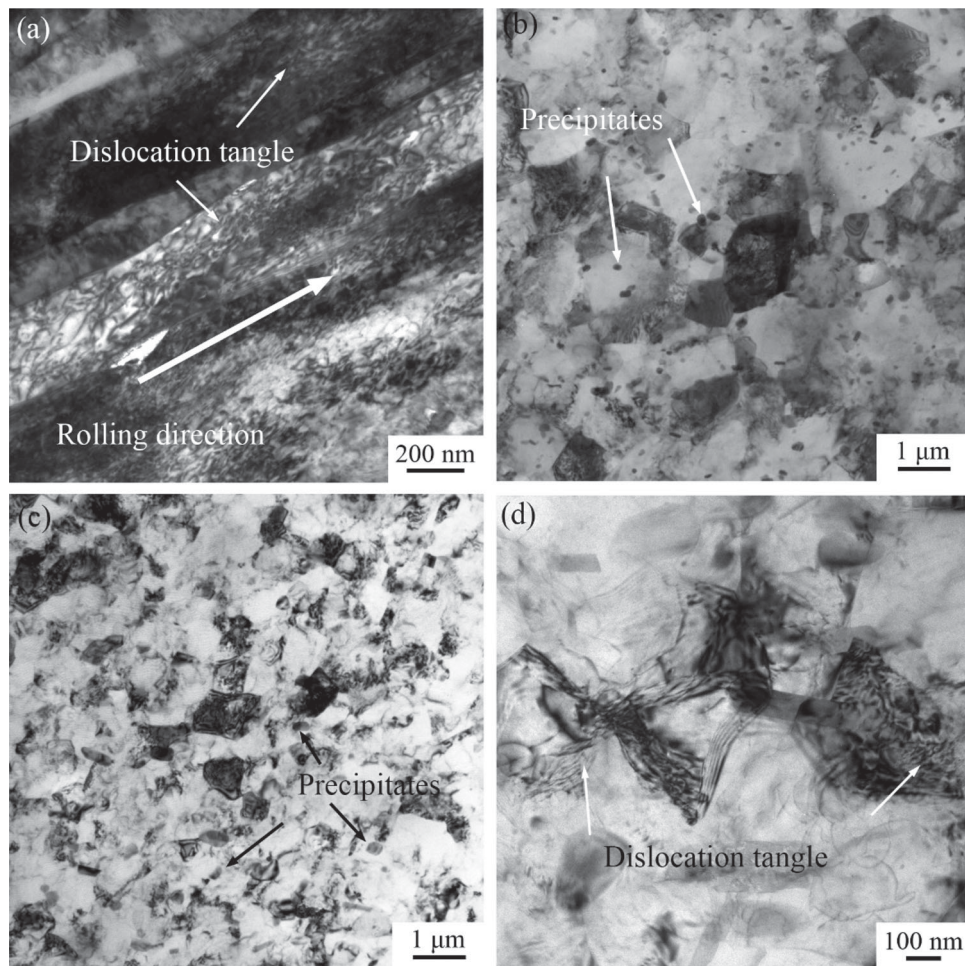
Figure 2. TEM microstructures of (a) BM and NZs of FSW joints: (b) A-200 sample, (c) W-200 sample, (d) magnified image of W-200 sample.

experimentally observed that Mg atoms easily segregated to grain boundaries under plastic deformation [15]. Straumal et al. [16] revealed the presence of the β-phase (Al_3Mg_2) particles in an Al-5wt-% Mg alloy after high-pressure torsion deformation through the selected area diffraction analysis. Therefore, the sphere-shaped particles in the NZ of the A-200 sample should be β-phase precipitates according to previous studies [16,17]. As a solution-strengthened 5xxx series Al alloy, the formation of the second phase particles will lead to the strength loss. Meanwhile, the high density of dislocations was mostly eliminated due to the strong annealing effect during the FSW thermal cycle. In this case, obvious softening should be achieved in the NZ of the A-200 sample, compared to that of the BM.

Under additional rapid water cooling, the average grains size was greatly refined to about 800 nm in the NZ of the W-200 sample, and few precipitates were observed, as shown in Figure 2(c). Moreover, it is found that the dislocation density increased in the NZ of the W-200 sample compared to the A-200 sample, and many dislocation sub-structures like cells and sub-grains were observed clearly (Figure 2(d)). This should be attributed to the reserved dislocation structures after

Table 1. Average grain size in the NZs and mechanical properties of the BM and FSW joints.

Sample	Grain size in NZ (μm)	Lowest hardness (HV)	YS (MPa)	UTS (MPa)	Elongation (%)
BM	–	125.5±1.9	370.3±3.1	425.1±3.7	5.7±0.3
A-200	1.8±0.9	95.4±0.8	260.4±1.7	344.3±1.6	4.8±0.2
W-200	0.8±0.5	115.2±1.1	340.2±3.6	403.0±2.4	3.5±0.2

the dynamic recrystallisation process, caused by the low welding temperature and rapid cooling rate.

All the FSW joints failed at the lowest hardness zone (LHZ) during the tensile tests, and the mechanical properties of the BM and FSW joints are shown in Table 1. Figure 3 summarises the experimental data on the joint coefficient versus strength of BM from the various FSW 5083 Al alloy joints reported in the present study and previous studies [18–23]. It is obvious that compared with other research results, very high joint coefficient was achieved in a BM with relatively high strength in the present study, which was attributed to the significantly reduced softening effect by using the low rotation rate with additional water cooling during FSW process.
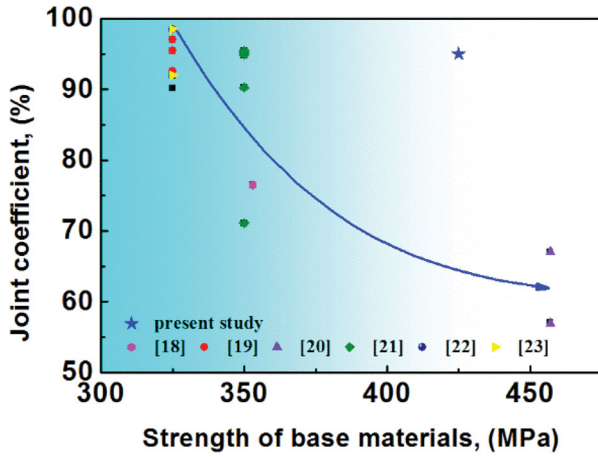
Figure 3. The joint coefficient and strength of BM for various FSW 5083Al alloy joints.
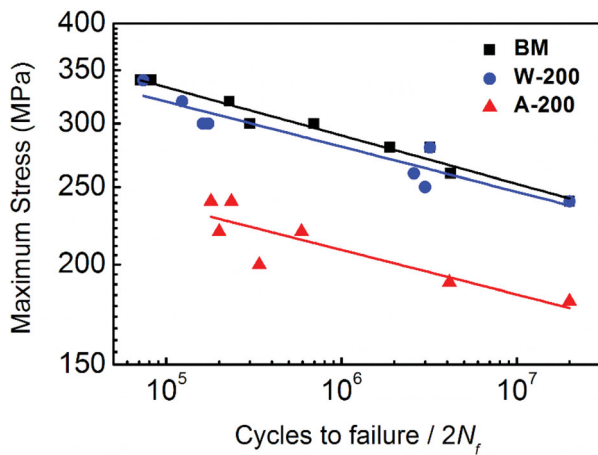

Figure 4. log-log formed stress-fatigue life (S-N) curves for BM and FSW joints.

High-cycle fatigue properties

The maximum stress-number of cycles to failure (S-N) curves by the log–log form of the BM and FSW joints are shown in Figure 4. Due to the work-hardening effect of cold rolling, the BM has a high fatigue limit (10^7 cycles) of 240 MPa, while the fatigue limit of the A-200 sample was greatly reduced to about 180 MPa. Therefore, the fatigue limit only reached 75% of the BM, though a relatively low heat input (rotation rate of 200 rpm) parameter was used when compared to the previous studies [1,12]. With further decreasing the heat input by applying the additional water cooling, a fatigue limit of 240 MPa was achieved in the W-200 sample, reaching to the BM level.

The relationship between the fatigue stress amplitude σ_a and fatigue life $2N_f$ can be expressed by the following Basquin equation:

$$\sigma_a = \sigma'_f (2N_f)^b \qquad (1)$$

where N_f is the fatigue life, σ'_f is the fatigue strength coefficient and b is the fatigue strength exponent (Basquin exponent), which are associated closely with
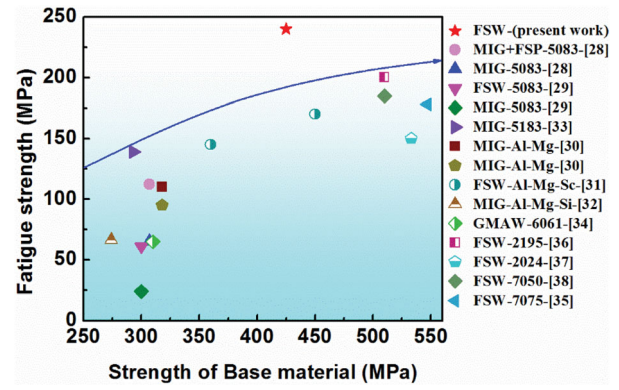
the material properties[24,25]. According to the fitting lines in Figure 4, the σ'_f of the BM was 668 MPa, and near σ'_f of 612 MPa was achieved in the W-200 sample. For the A-200 sample, the σ'_f greatly decreased to 450 MPa. The b value of the BM was −0.059, which was a little lower than that of both FSW joints (−0.056).

Usually, the σ'_f is nearly equal to the true tensile strength after modification with necking and b represents the degree of the fatigue damage, which is associated with the initial microstructure characteristics [26,27]. Compare with the BM, the σ'_f of the A-200 sample decreased clearly but the similar b value was obtained, so the fatigue limit was reduced to 180 MPa. For the W-200 sample, despite a slightly decreased σ'_f of 612 MPa, the b value increased to −0.056. Therefore, the same fatigue limit to the BM (240 MPa) can be achieved. A comparison of the fatigue strength for various Al alloy joints under different welding processes and BM strength in present work and previous studies is shown in Figure 5 [28–38]. It can be found that the fatigue strength increases as increasing the BM strength. The fatigue strength of most Al alloy joints was lower than 200 MPa, and all the date points located under a blue curve as shown in Figure 5. However, the data point of FSW Al alloy joint in this study clearly separated from the curve, showing higher fatigue properties compared to other Al alloy joints.

Fatigue fracture behaviour

The typical cross-section morphologies of the fractured samples after fatigue tests are shown in Figure 6. Interestingly, the fracture locations of both FSW joints were not at the LHZs which are located in the HAZs. As can be seen from Figure 6, all the A-200 samples fractured at the NZ, while the W-200 samples fractured at the BM far away from the NZ. The applying of additional water cooling can not only improve the fatigue limit of the FSW joint but also change the fracture location from the NZ to the BM. Thought the additional water cooling
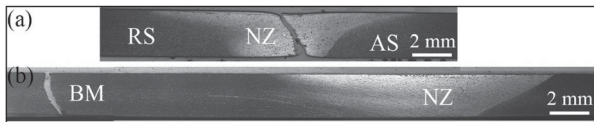

Figure 5. Fatigue strength and strength of BM for various Al alloy joints.

Figure 6. Fractured samples of FSW joints: (a) A-200 sample, (b) W-200 sample.

Figure 7. Hardness distributions of FSW 5083Al-H19 joints.

changed the distribution of 'S' line, the existence of 'S' line does not affect the fatigue properties of FSW joints.

Usually, there are two possible reasons for this exceptional fracture phenomenon: the effect of residual stress or the HAZ strengthening under cyclic stress. It is well accepted that the fatigue crack growth in the FSW joints was influenced both by the applied stress from the external cyclic loading and by the internal residual stress, and the later usually plays an important role [10].

Previous studies indicated that the NZ usually showed the highest tensile residual stress and the HAZ showed a compressive residual stress or lower tensile residual stress at transverse direction [20,39]. The transverse residual is parallel to the fatigue loading direction and effects the fatigue property. Under a tension-tension cyclic deformation mode in this study, compressive residual stress in the transverse direction would decrease the loading stress and the tensile residual stress played an opposite role. Therefore, the higher tensile residual stress in the NZ in the transverse direction resulted in the worse fatigue tolerance of the NZ than that of the HAZ.

Besides the residual stress, the strengthening of the HAZ is also a probable reason for the unusual fracture phenomenon. When deformed under cyclic loading, the special structure of the FSW joints inevitably leads to inhomogeneity deformation. At the initial stage during the fatigue test, the HAZ may be strengthened through the accumulation of dislocations under the cyclic deformation. If the HAZ is strengthened to the same or higher level of the NZ or the BM, the fracture would occur in the NZ or the BM instead of the HAZ at the final fracture stage.

In order to verify if the HAZ was strengthened during the fatigue process, the microhardness profiles of the FSW joints were measured on the cross-section before and after fatigue tests, as shown in Figure 7. It is clear that two LHZs can be observed from the hardness distribution, which was located at both sides of the HAZs. However, the lowest hardness values of the A-200 and W-200 samples almost the same before and after fatigue tests, indicating that no obvious strengthening occurred in the HAZs. On the contrary, obvious hardness changes can be observed in the NZ especially for the A-200 sample. Obviously, local deformation occurred preferentially in the NZs of both samples during the cyclic deformation. Therefore, the exceptional phenomenon cannot be attributed to the HAZ

strengthening, but more probably associated with the residual stress.

For the A-200 sample, the hardness increased clearly in the NZ, and the weld centre exhibited the highest hardness value of about 130 HV. For the W-200 sample, though the enhanced amplitude decreased significantly in the NZ, the change mode was similar to that of the A-200 sample. Obviously, local deformation occurred preferentially in the NZs of both samples during the cyclic deformation. Therefore, the exceptio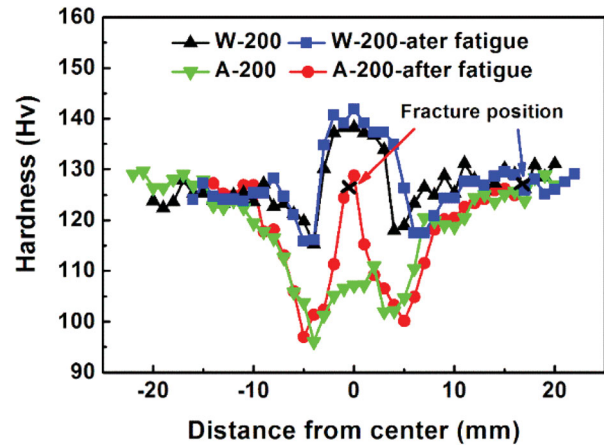nal phenomenon cannot be attributed to the HAZ strengthening, but more probably associated with the residual stress. For the A-200 sample, the hardness value in the NZ was only 10 HV higher than that of the HAZ, so this difference was too little compared to the effect of the residual stress. Then, preferential local deformation occurred in the NZ under the enhanced tensile effect of the residual stress, and finally failed in this zone. For the W-200 sample, the hardness value in the NZ was much higher than that of the BM and HAZ, which was due to the grain refinement. In our previous study, we found that the hardness value increased with decreasing grain size, and followed the Hall-Petch relationship [11]. Though local deformation occurred in the NZ at the initial stage, fracture did not occur in this zone. For the HAZ of the W-200 sample, the hardness value was only 10 HV lower than that of the BM. However, decreased tensile effect from the residual stress in the HAZ greatly improved the fatigue performance which was even higher than that of the BM, so the final fracture occurred at the BM.

Crack initiation and propagation

Figure 8 shows the typical fracture surface of the BM and A-200 joint after fatigue test, which reveals conventional three regions of crack initiation, stable growth and final fracture zones. The small crack initiation zone that is located at the sample surface is relatively flat due to the repeated friction of fractured surface during cyclic deformation, as shown in Figure 8(b,f). It was
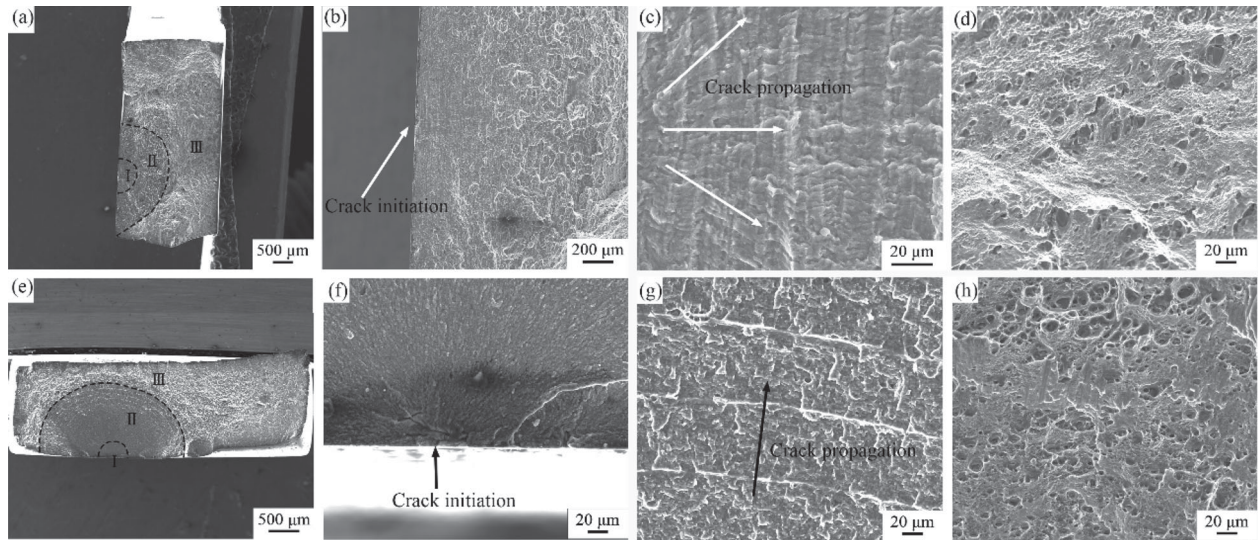
Figure 8. Fractured surface morphologies of BM at a maximum stress of 280 MPa: (a) macroscopic feature, (b) crack initiation zone (region I), (c) crack propagation zone (region II), (d) final fracture zone (region III), and A-200 joint at a maximum stress of 240 MPa: (e) macroscopic feature, (f) crack initiation zone (region I), (g) crack propagation zone (region II), (h) final fracture zone (region III).
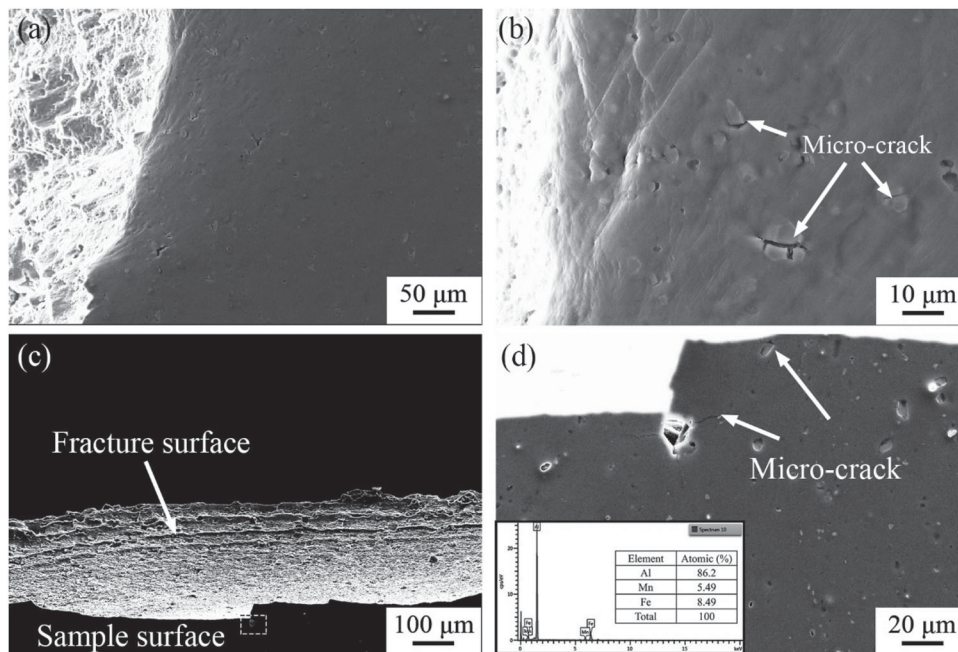

Figure 9. Surface damage morphologies of BM and A-200 sample: (a) BM at a maximum stress of 340 MPa, (b) magnified image of the rectangle in a, (c) A-200 sample at a maximum stress of 200 MPa, (d) magnified image of the rectangle in c.

found that the crack initiation site was not at the root of the NZ but located at the sample surface, indicating the sound FSW joint was achieved. In the crack propagation zone, there are no obvious fatigue striations due to the relatively low ductility of the BM (Figure 8(c)). For A-200 joint, there are many beaches or clam shell markings on the fracture surfaces can display the direction of fatigue crack propagation (Figure 8(g)). The surface characteristic of the final fracture zone was similar to that of the tensile fractographs with shallow dimples, as exhibited in Figure 8(d,h). However, the dimple density was definitely more in A-200 joint than that of the BM sample, indicating the enhanced plasticity in the NZ. The W-200 sample fractured at the BM zone, so the

fatigue fracture characteristics were the same as those for the BM sample.

Surface damage morphologies of the BM and FSW joints are shown in Figure 9. It is clear that many microscopic cracks and debonding at the impurity particles/matrix interfaces were observed on the surface of BM and A-200 samples. EDS analyses of the A-200 sample and BM showed that the coarse particles contained higher Mn, Fe elements (Figure 9(d)), indicating that the particles should be $Al_6(Mn,Fe)$ which was commonly reported in previous studies [17,40]. The impurity particles play important roles in the crack initiation and propagation during cyclic deformation [41], and micro-crack should easily initiate at the impurity

particle/matrix interface [42]. This indicated that preferential deformation resulted in a highly localised stress concentration on the impurity particles, which led to early nucleation of fine microscopic cracks.

Conclusions

High-cycle fatigue behaviour of FSW 5083Al-H19 joints was investigated in this study. Through the additional water cooling, high property FSW joint with equal fatigue strength to the BM was achieved and the FSW joints showed different fatigue fracture behaviours. The following conclusions can be obtained.

(1) For a normal FSW joint (A-200), fine equiaxed grains with plenty β phase particles were obtained in the NZ. By applying additional water cooling, ultrafine grains with high dislocation density were obtained in the NZ for the W-200 sample, and only few β phase particles were observed.

(2) The joint efficiency increased from 81% for the A-200 sample to 95% for the W-200 sample, which was attributed to the significantly reduced softening effect in the HAZ under the additional water cooling.

(3) The fatigue limit increased from 180 MPa for the A-200 sample to 240 MPa for the W-200 sample which was equal to that of the BM. Fatigue samples did not fail in the LHZ, but in the NZ and BM for the A-200 sample and W-200 sample, respectively.

Disclosure statement

No potential conflict of interest was reported by the authors.

Funding

References

[1] Mishra RS, Ma ZY. Friction stir welding and processing. Mater Sci Eng R. 2005;50:1–78.

[2] Lombard H, Hattingh DG, Steuwer A, et al. Optimising FSW process parameters to minimise defects and maximise fatigue life in 5083-H321 aluminium alloy. Eng Fract Mech. 2008;75:341–354.

[3] Xue P, Xiao BL, Zhang Q, et al. Achieving friction stir welded pure copper joints with nearly equal strength to the parent metal via additional rapid cooling. Scripta Mater. 2011;64:1051–1054.

[4] Sharma C, Dwivedi DK, Kumar P. Influence of in-process cooling on tensile behaviour of friction stir welded joints of AA7039. Mater Sci Eng A. 2012;556:479–487.

[5] Zeng XH, Xue P, Wang D, et al. Realising equal strength welding to parent metal in precipitation-hardened Al-Mg-Si alloy via low heat input friction stir welding. Sci Tech Weld Join. 2018;23:478–486.

[6] Fujii H, Chung YD, Sun YF. Friction stir welding of AISI 1080 steel using liquid CO2 for enhanced toughness and ductility. Sci Tech Weld Join. 2013;18:500–506.

[7] Zhou C, Yang X, Luan G. Effect of kissing bond on fatigue behavior of friction stir welds on Al 5083 alloy. J Mater Sci. 2006;41:2771–2777.

[8] Zhou C, Yang X, Luan G. Effect of root flaws on the fatigue property of friction stir welds in 2024-T3 aluminum alloys. Mater Scie Eng A. 2006;418: 155–160.

[9] Ni DR, Chen DL, Xiao BL, et al. Residual stresses and high cycle fatigue properties of friction stir welded SiCp/AA2009 composites. Int J Fatigue. 2013;55:64–73.

[10] Bussu G, Irving PE. The role of residual stress and heat affected zone properties on fatigue crack propagation in friction stir welded 2024-T351 aluminium joints. Int J Fatigue. 2003;25:77–88.

[11] Besel M, Besel Y, Alfaro Mercado U, et al. Fatigue behavior of friction stir welded Al–Mg–Sc alloy. Int J Fatigue. 2015;77:1–11.

[12] Wang BB, Chen FF, Liu F, et al. Enhanced mechanical properties of friction stir welded 5083Al-H19 joints with additional water cooling. J Mater Sci Technol. 2017;33:1009–1014.

[13] Sato YS, Yamashita F, Sugiura Y, et al. FIB-assisted TEM study of an oxide array in the root of a friction stir welded aluminium alloy. Scripta Mater. 2004;50:365–369.

[14] Zeng XH, Xue P, Wang D, et al. Material flow and void defect formation in friction stir welding of aluminium alloys. Sci Technol Weld Join. 2018;23:677–686.

[15] Liu Y, Liu M, Chen X, et al. Effect of Mg on microstructure and mechanical properties of Al-Mg alloys produced by high pressure torsion. Scripta Mater. 2019;159:137–141.

[16] Straumal BB, Baretzky B, Mazilkin AA, et al. Formation of nanograined structure and decomposition of supersaturated solid solution during high pressure torsion of Al–Zn and Al–Mg alloys. Acta Mater. 2004;52:4469–4478.

[17] Yan J, Hodge AM. Study of β precipitation and layer structure formation in Al 5083: The role of dispersoids and grain boundaries. J Alloys Compd. 2017;703:242–250.

[18] Paik J-K. Mechanical properties of friction stir welded aluminum alloys 5083 and 5383. Int J Nav Arch Ocean. 2009;1:39–49.

[19] Birol Y, Kasman S. Effect of welding parameters on microstructure and mechanical properties of friction stir welded EN AW 5083 H111 plates. Mater Sci Technol. 2013;29:1354–1362.

[20] Peel M, Steuwer A, Preuss M, et al. Microstructure, mechanical properties and residual stresses as a function of welding speed in aluminium AA5083 friction stir welds. Acta Mater. 2003;51:4791–4801.

[21] Hirata T, Oguri T, Hagino H, et al. Influence of friction stir welding parameters on grain size and formability in 5083 aluminum alloy. Mater Sci Eng A. 2007;456:344–349.

[22] Han MS, Lee SJ, Park JC, et al. Optimum condition by mechanical characteristic evaluation in friction stir welding for 5083-O Al alloy. T Nonferr Metal Soc. 2009;19:S17–S22.

[23] Kasman S, Kahraman F. Investigations for the effect of parameters on the weld performance of AA 5083-H111 joined by friction stir welding. P I Mech Eng B-J Eng. 2014;228:937–946.

[24] An XH, Wu SD, Wang ZG, et al. Significance of stacking fault energy in bulk nanostructured materials: Insights from Cu and its binary alloys as model systems. Prog Mater Sci. 2019;101:1–45.

[25] An X, Lin Q, Wu S, et al. Improved fatigue strengths of nanocrystalline Cu and Cu–Al alloys. Mater Res Lett. 2015;3:135–141.

[26] Xue P, Huang Z, Wang B, et al. Intrinsic high cycle fatigue behavior of ultrafine grained pure Cu with stable structure. Sci China Mater. 2016;59:531–537.

[27] Xue P, Wang BB, An XH, et al. Improved cyclic softening behavior of ultrafine-grained Cu with high microstructural stability. Scripta Mater. 2019;166:10–14.

[28] Borrego LP, Costa JD, Jesus JS, et al. Fatigue life improvement by friction stir processing of 5083 aluminium alloy MIG butt welds. Theor Appl Fract Mec. 2014;70:68–74.

[29] Zhou C, Yang X, Luan G. Fatigue properties of friction stir welds in Al 5083 alloy. Scripta Mater. 2005;53:1187–1191.

[30] Yan S, Nie Y, Zhu Z, et al. Characteristics of microstructure and fatigue resistance of hybrid fiber laser-MIG welded Al–Mg alloy joints. Appl Surf Sci. 2014;298:12–18.

[31] Zhemchuzhnikova D, Mironov S, Kaibyshev R. Fatigue performance of friction-stir-welded Al-Mg-Sc Alloy. Metall Mater Trans A. 2016;48:150–158.

[32] Lin S, Deng Y-L, Tang J-G, et al. Microstructures and fatigue behavior of metal-inert-gas-welded joints for extruded Al-Mg-Si alloy. Mater Sci Eng A. 2019;745:63–73.

[33] Gaur V, Enoki M, Okada T, et al. A study on fatigue behavior of MIG-welded Al-Mg alloy with different filler-wire materials under mean stress. Int J Fatigue. 2018;107:119–129.

[34] Ambriz RR, Mesmacque G, Ruiz A, et al. Effect of the welding profile generated by the modified indirect electric arc technique on the fatigue behavior of 6061-T6 aluminum alloy. Mater Sci EngA. 2010;527:2057–2064.

[35] Uematsu Y, Tokaji K, Shibata H, et al. Fatigue behaviour of friction stir welds without neither welding flash nor flaw in several aluminium alloys. Int J Fatigue. 2009;31:1443–1453.

[36] Moreira PMGP, de Jesus AMP, de Figueiredo MAV, et al. Fatigue and fracture behaviour of friction stir welded aluminium–lithium 2195. Theor Appl Fract Mec. 2012;60:1–9.

[37] Vidal C, Infante V, Vilaça P. Assessment of improvement techniques effect on fatigue behaviour of friction stir welded aerospace aluminium alloys. Procedia Engineer. 2010;2:1605–1616.

[38] Deng C, Wang H, Gong B, et al. Effects of microstructural heterogeneity on very high cycle fatigue properties of 7050-T7451 aluminum alloy friction stir butt welds. Int J Fatigue. 2016;83:100–108.

[39] Linton VM, Ripley MI. Influence of time on residual stresses in friction stir welds in agehardenable 7xxx aluminium alloys. Acta Materi. 2008;56:4319–4327.

[40] Luo T, Ni DR, Xue P, et al. Low-temperature superplasticity of nugget zone of friction stir welded Al-Mg alloy joint. Mater Sci Eng A. 2018;727:177–183.

[41] Sun G, Wang C, Wei X, et al. Study on small fatigue crack initiation and growth for friction stir welded joints. Mater Sci Eng A. 2019;739:71–85.

[42] Wang W, Qiao K, Wu JL, et al. Fatigue properties of friction stir welded joint of ultrafine-grained 2024 aluminium alloy. Sci Technol Weld Join. 2017;22:110–119.